

## Effect of white mud on properties of alkali activated slag

Sun, Renjuan; Bu, Linglai; Zhang, Hongzhi; Guan, Yanhua; Ma, Chuanyi; Ge, Zhi; Šavija, Branko

**DOI**

[10.1016/j.conbuildmat.2023.131944](https://doi.org/10.1016/j.conbuildmat.2023.131944)

**Publication date**

2023

**Document Version**

Final published version

**Published in**

Construction and Building Materials

**Citation (APA)**

Sun, R., Bu, L., Zhang, H., Guan, Y., Ma, C., Ge, Z., & Šavija, B. (2023). Effect of white mud on properties of alkali activated slag. *Construction and Building Materials*, 392, Article 131944. <https://doi.org/10.1016/j.conbuildmat.2023.131944>

**Important note**

To cite this publication, please use the final published version (if applicable). Please check the document version above.

**Copyright**

Other than for strictly personal use, it is not permitted to download, forward or distribute the text or part of it, without the consent of the author(s) and/or copyright holder(s), unless the work is under an open content license such as Creative Commons.

**Takedown policy**

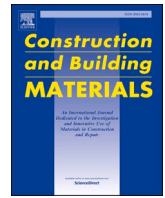
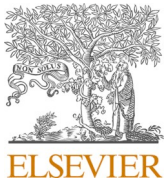
Please contact us and provide details if you believe this document breaches copyrights. We will remove access to the work immediately and investigate your claim.

***Green Open Access added to TU Delft Institutional Repository***

***'You share, we take care!' - Taverne project***

**<https://www.openaccess.nl/en/you-share-we-take-care>**

Otherwise as indicated in the copyright section: the publisher is the copyright holder of this work and the author uses the Dutch legislation to make this work public.



## Effect of white mud on properties of alkali activated slag

Renjuan Sun<sup>a</sup>, Linglai Bu<sup>a</sup>, Hongzhi Zhang<sup>a,b,\*</sup>, Yanhua Guan<sup>a</sup>, Chuanyi Ma<sup>c</sup>, Zhi Ge<sup>a</sup>, Branko Šavija<sup>d</sup>

<sup>a</sup> School of Qilu Transportation, Shandong University, 250002 Jinan, PR China

<sup>b</sup> Suzhou Research Institute, Shandong University, 215021 Suzhou, PR China

<sup>c</sup> Shandong Hi-Speed Engineering Test CO., LTD, 250002 Jian, PR China

<sup>d</sup> Microlab, Faculty of Civil Engineering and Geosciences, Delft University of Technology, 2628 CN Delft, The Netherlands

### ARTICLE INFO

#### Keywords:

Alkali activated slag  
White mud  
Hydration products  
Microstructure

### ABSTRACT

White mud is a solid waste from the papermaking industry, composed mainly of  $\text{CaCO}_3$  and residual alkali metal ions (such as  $\text{Na}^+$ ,  $\text{Mg}^{2+}$ ). In the current study, the feasibility of using white mud as partial replacement of slag in alkali activated materials is explored. The fluidity, setting time, autogenous shrinkage, mechanical properties, hydration products and microstructure of alkali activated slag containing different amount of white mud are studied. The results show that adding white mud reduces the fluidity of freshly mixed paste, setting time and autogenous shrinkage. The ions released from the white mud participate in the polymerization reaction, accelerate the hydration reaction in the early stage, and promotes the precipitation of Mg-Al and the formation of hydrotalcite. However, excessive quantities of white mud (above 15% of the binder) leads to the reduction of compressive strength. As the content of white mud is enhanced, the Ca/(Si + Al) ratio of the gel increases and the degree of polymerization is reduced. It has been shown that white mud has potential reactivity and can partially replace slag to prepare new alkali activated materials.

### 1. Introduction

Cement production results in a large amount of carbon dioxide, accounting for approximately 8–9% of global  $\text{CO}_2$  emissions [1]. Cement production is also energy-intensive: production of 1 ton of cement requires about 110 kWh of electricity [2]. In addition, it generates a substantial amount of noise and dust. Consequently, there is an urgent need for the development of low-energy and low-carbon binders to reduce the use of cement clinker [3,4].

Alkali-activated materials (AAMs), as alternative binders to ordinary Portland cement (OPC), are low-carbon cementitious materials because they have low natural resource consumption and reduced carbon dioxide emissions [5–7]. AAMs are composed of aluminosilicate precursors and alkaline activators, which can be produced without calcination. Different industrial by-products or solid wastes can be used as precursors, including granulated blast furnace slag [8,9], metakaolin [10], fly ash [11], natural volcanic ash [12], waste rocks [13], flue gas desulfurization (FGD) residue [14], red mud [15,16], waste glass [17,18], tailings [19], bottom ash [20] and limestone [21–23], etc. Among them, ground granulated blast furnace slag (GGBFS) has high

reactivity, allowing it to react in a mild alkaline environment [24]. Therefore, less strong alkali can be used in the production of alkali activated slag, saving costs, and solving the problem of activator causticity. Therefore, alkali activated slag (AAS) has been widely studied as an environmentally friendly construction material. It can be used for backfilling, rapid pavement repair, wastewater adsorption, etc. However, AAS has high shrinkage and cracking [23,25,26], which limits its practical use. The properties of AAS are significantly influenced by the incorporation of other precursors [27]. Different precursors have been developed and blended with slag to overcome the drawbacks of AAS. Najimi et al. [28] studied the engineering properties of alkali-activated natural pozzolan/slag concrete and provided the optimum precursor and activator combinations. It was reported by Egodagamage et al. [29] that using biochar as a partial replacement of GGBFS promoted the hydration reaction and increased the compressive strength of AAS. According to Li et al. [30], incorporation of metakaolin mitigated the autogenous shrinkage and increased the flexural strength of AAS. Rakhimova et al. [21] found that introduction of limestone in AAS improved the physical structure and compressive strength of alkali-activated slag paste. Among them, limestone powder (LSP) can be

\* Corresponding author at: School of Qilu Transportation, Shandong University, 250002 Jinan, PR China.

E-mail address: [hzzhang@sdu.edu.cn](mailto:hzzhang@sdu.edu.cn) (H. Zhang).

<https://doi.org/10.1016/j.conbuildmat.2023.131944>

Received 22 January 2023; Received in revised form 4 May 2023; Accepted 23 May 2023

Available online 30 May 2023

0950-0618/© 2023 Elsevier Ltd. All rights reserved.

found almost everywhere in the world. Therefore, attention has been paid to apply LSP in alkali activated materials [23].

Limestone, mainly composed of  $\text{CaCO}_3$ , can not only fill the porosity in the AAS system and enhance the microstructural density, but also has a chemical modification effect [22]. Some researchers [23,31] analyzed the exothermic process of AAS system blend with limestone addition by isothermal calorimetry and found that the application of limestone improved the reaction rate. Dai et al. [32] observed, through pore solution chemical analysis, that limestone could promote the dissolution of  $\text{Ca}^{2+}$  and  $\text{Al}^{3+}$  in the precursors, thus accelerating the reaction. Xiang et al [26] indicated that the appropriate amount of  $\text{CaCO}_3$  can improve the rheological properties, reduce drying shrinkage, increase the density of the matrix and accelerate the reaction, thus promoting the strength development. Marsh et al. [33] reported that limestone addition accelerates reaction in  $\text{Na}_2\text{SO}_4$ -activated GGBS.

White mud is a by-product of the alkali recovery process from the paper industry. The composition of white mud is similar to limestone whose main component is calcium carbonate. White mud also contains residual alkali metal ions (such as  $\text{Na}^+$ ,  $\text{Mg}^{2+}$ ), which is alkaline [34,35]. However, compared with limestone, the use of white mud in the field of building materials has not been extensively studied. Ingale et al. [36] investigated properties of fresh concrete made with white mud and GGBS as cement replacement and observed that white mud increased the water demand. Phan et al. [37] demonstrated that white mud improved the stability of high-water-content clays immediately after mixing owing to its good water absorption and retention performance. Although white mud can also be applied in wastewater treatment, gas adsorption, and bio additives, these approaches do not consume white mud on a large scale [38]. Most of the white mud is still landfilled, causing serious damage to the environment [39]. Production of 1 ton of paper products results in 1.63 tons of white mud [38]. As the largest papermaking country in the world, the annual output of white mud in China exceeds 80 million tons [40], which makes the paper industry one of the most polluting industries. Therefore, the effective treatment and utilization of white mud is of great significance.

To this end, the current study investigates the feasibility of utilizing white mud for partial replacement of slag to prepare new alkali activated slag and analyzes the effect of residual ions from white mud on development of macroscopic properties and microstructure of AAS. It is expected that the current study can facilitate the practical application of white mud in AAMs.

## 2. Materials and experiments

### 2.1. Raw materials and mixture proportions

The materials used are S95 ground granulated blast furnace slag (GGBFS) and white mud supplied by Liaocheng paper mill, Shandong province. Chemical compositions of GGBFS and white mud were determined by X-ray fluorescence, see Table 1. The GGBFS is rich in Si and Al and consists mainly of amorphous glass phase. The mineral composition and particle size distribution are shown in Fig. 1 and Fig. 2, respectively. It has a specific surface area of  $1.339 \text{ m}^2/\text{g}$  and a median particle size of  $17.568 \mu\text{m}$ . The main mineral component of white mud is calcite. The white mud is a bit finer than GGBFS and possesses a specific surface area of  $4.628 \text{ m}^2/\text{g}$  and a median particle size of  $11.482 \mu\text{m}$ . A scanning electron microscopy (SEM) images of GGBFS and white mud are shown in Fig. 3. GGBFS particles are irregular and white mud has a porous structure.

**Table 1**

Chemical composition of raw materials by XRF.

Oxide (wt%)	CaO	$\text{SiO}_2$	$\text{Al}_2\text{O}_3$	$\text{Na}_2\text{O}$	MgO	LOI	Other
GGBFS	39.69	31.34	16.67	1.80	2.26	6.14	2.10
White mud	47.50	2.08	0.71	2.80	2.74	42.84	1.33

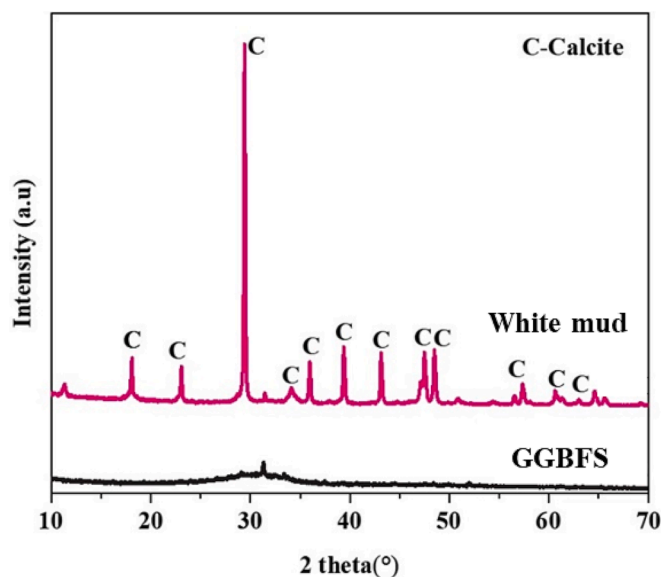


**Fig. 1.** XRD patterns of raw materials (C = Calcite).

The mix proportion of Alkali activated white mud/slag (AAWS) is shown in Table 2. Fourteen different AAWS pastes were designed. The adopted liquid to solid weight ratio was 0.35 and the mass ratio of  $\text{Na}_2\text{O}$  to solid was 5.6%. The white mud addition was varied by replacing different amounts of GGBFS. The white mud contents of SH0, SH5 and SH10 were 0%, 5% and 10%, respectively. Two types of alkali activator were considered. SH refers to the samples activated by sodium hydroxide solution and SS indicates the specimens activated by water glass solution.

The activator was prepared by mixing anhydrous pellets of sodium hydroxide with distilled water and sodium silicate solution. The solution was allowed to cool down for 24 h to room temperature ( $20 \pm 2 \text{ }^\circ\text{C}$ ) before mixing with the precursors. A Planetary mixer with a capacity of 1L was used for mixing. After premixing of the raw materials for 5 min under low speed, the activator was added and mixed at high speed for 2 min. The mix was used for the further test.

### 2.2. Experimental methods

#### 2.2.1. Fluidity

The fluidity of AAWS paste was tested according to Chinese standard GB/T 8077–2012. The mixed AAWS paste was poured into the truncated cone round mold (upper diameter: 36 mm; lower diameter: 60 mm; height: 60 mm). The paste was scraped with a scraper, then the mould was lifted in the vertical direction and the stopwatch was turned on at the same time. After 30 s, a ruler was used to measure the maximum diameter in two perpendicular directions and the average value was taken as the fluidity.

#### 2.2.2. Setting time

Based on the Chinese standard GB/T1346-2011, the initial setting and final setting of AAWS paste were measured by the Vicat apparatus. The Vicat mould has an internal diameter of 75 mm at the base and 65 mm at the top, with a height of 40 mm. The initial setting was defined when the Vicat needle sunk into 4 mm from the base plate. Final setting was determined as when the ring attachment starts to leave no visible traces on the sample. It was measured every 30 s.

#### 2.2.3. Compressive strength

For the compressive strength measurements, specimens with size of  $40 \text{ mm} \times 40 \text{ mm} \times 40 \text{ mm}$  were used. The specimens were cured in a room with relative humidity of 95% and temperature of  $20 \pm 2 \text{ }^\circ\text{C}$

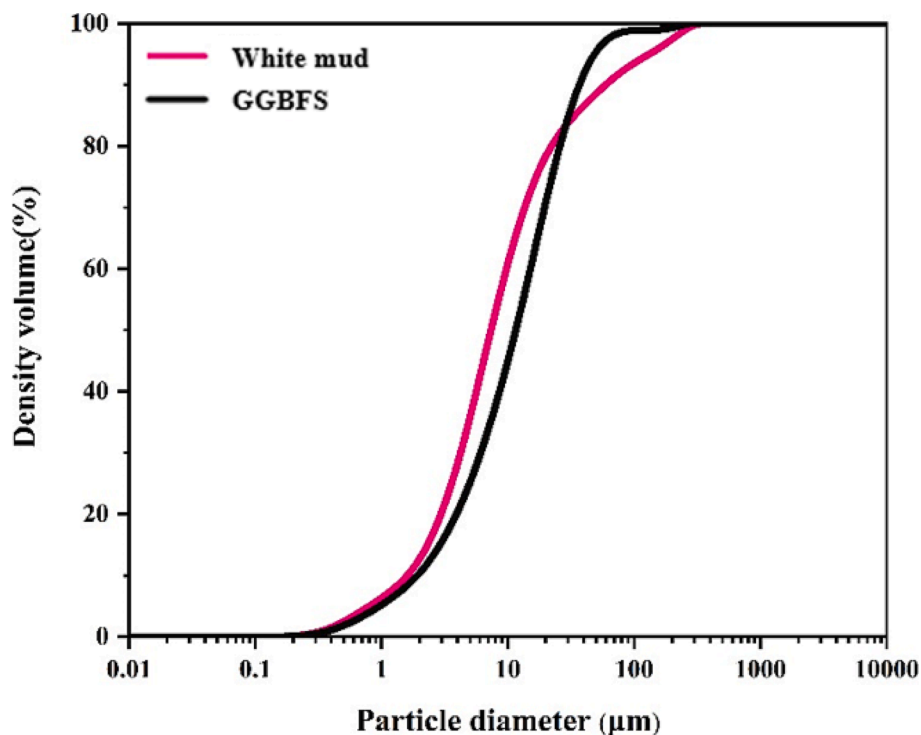
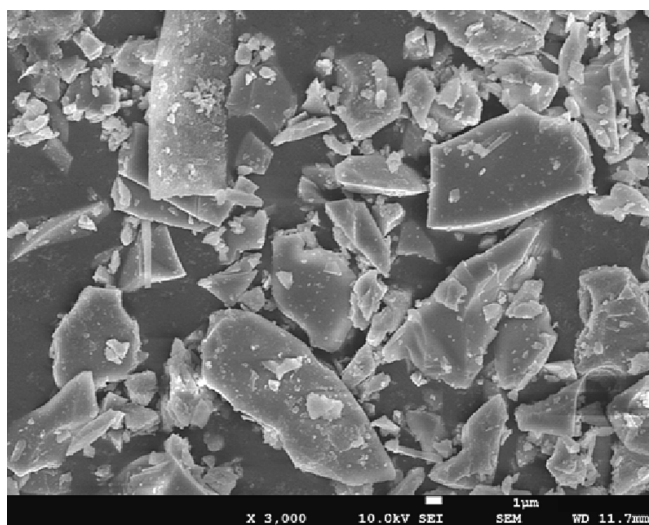
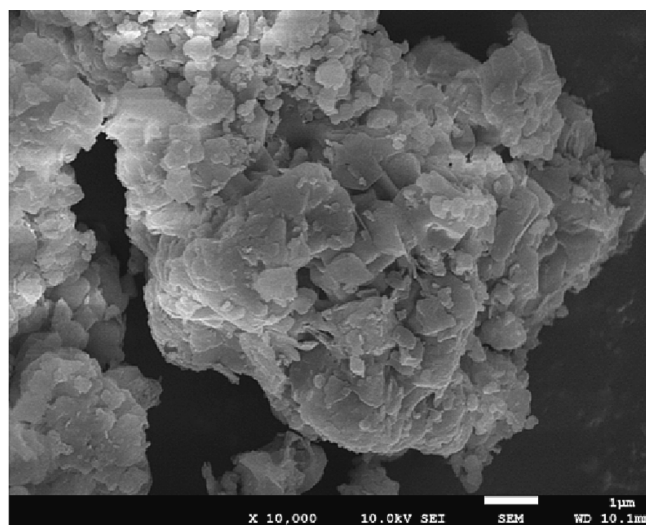


Fig. 2. Particle size distribution of GGBFS and white mud.



(a)



(b)

Fig. 3. Scanning electron microscopy (SEM) image of (a) GGBFS and (b) white mud.

according to the standard (Chinese standard GB/T 17671–1999) until testing (1d, 7d and 28d). The specimen was loaded with a constant rate of 1 kN/s. The average value of three specimens for each mix was taken as the compressive strength.

#### 2.2.4. X-ray diffraction test

X-ray diffraction (XRD) measurements were conducted to examine the chemical phase in the pastes. A Rigaku Dmax-2500PC powder X-ray diffractometer with Cu K $\alpha$  radiation was used. It was operated at 40 kV and 30 mA. A step size of 0.020° within the scanning range of 10–70° was adopted.

#### 2.2.5. Fourier transform infrared spectroscopy test

Fourier transform infrared spectroscopy (FTIR) measurement was performed with a Nicolet IS 10 FTIR spectrometer. The spectra were analyzed over the wavelength range from 600 to 2000  $\text{cm}^{-1}$  with a resolution of 4  $\text{cm}^{-1}$ . 32 scans were acquired for each measurement. The spectra were analytically derived using the PerkinElmer Spectrum 100 software.

#### 2.2.6. Thermogravimetric analysis

Thermogravimetric analysis (TGA) was conducted to identify the reaction products of AAWs. A TGA-5500 Thermogravimetric Analyzer was used. Samples were heated from room temperature (20 °C) to 950 °C at a heating rate of 10 °C/min. Nitrogen with a flow rate of 60

**Table 2**

Mix proportion of AAWS.

Code	GGBFS (wt %)	White mud (wt%)	Na <sub>2</sub> O (%)	Ms=(SiO <sub>2</sub> /Na <sub>2</sub> O)	Liquid/Solid
SH0	100	0	5.6	–	0.35
SH5	95	5			
SH10	90	10			
SH15	85	15			
SH20	80	20			
SH25	75	25			
SH30	70	30			
SS0	100	0	5.6	1.2	0.35
SS5	95	5			
SS10	90	10			
SS15	85	15			
SS20	80	20			
SS25	75	25			
SS30	70	30			

ml/min was used to create an inert environment. An empty alumina crucible was used as a control before the test, and the blank curve was subtracted to ensure accurate data.

### 2.2.7. Scanning electron microscopy

A JSM-7610F scanning electron microscope (SEM) equipped with an energy-dispersive X-ray spectroscopy detector was used to observe the morphology of AAWS using the secondary electron (SE) mode. An acceleration voltage of 15 kV was chosen. Before testing, the samples were first dried under vacuum conditions and sprayed using a high-resolution sputter coater with a spray layer of platinum for 360 s. Back scattered electron (BSE) mode and Energy dispersive spectroscopy (EDS) were used to characterize the microstructure of AAWS and to perform quantitative analysis of the reaction products. Prior to the test, dried samples were impregnated with epoxy resin. After hardening, the specimens were grinded with grit silicon carbide paper of 800 grit, 1200 grit, 2000 grit, and 4000 grit in order. They were then polished with diamond pastes with particle size of 9, 3, 1, and 0.25  $\mu$ m. The samples were washed regularly in an isopropanol ultrasonic bath after each polishing step. In the end, the well-polished samples were dried in a vacuum oven.

## 3. Results and discussion

### 3.1. Fluidity

The slump flow of the freshly mixed alkali white mud-slag paste is shown in Fig. 4. In general, at the same level of white mud replacement,

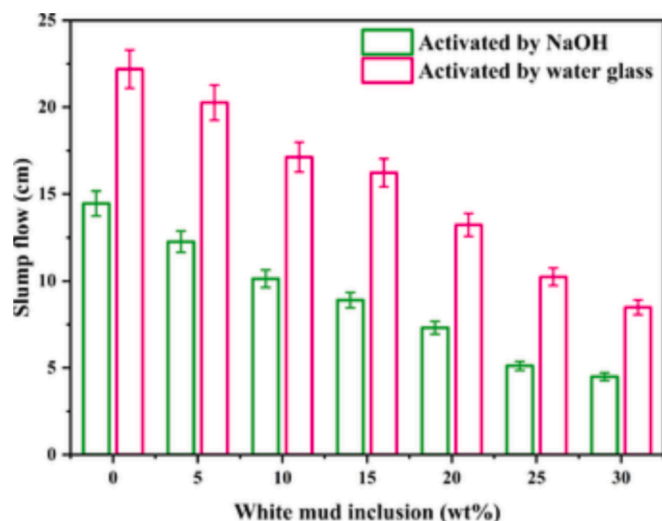


Fig. 4. Slump flow of AAWS pastes.

the samples activated by water glass exhibited much higher fluidity. This is due to the silicate ions contained in the water glass, which enhance the charge repulsion of the liquid phase on the particle surface. The incorporation of white mud reduced the fluidity of the paste of alkali activated slag. This is the opposite of the effect caused by the addition of limestone powder which has a similar mineral composition, i.e. calcite [23,26,32]. The reasons are as follows: 1) white mud has a larger specific surface area; 2) As shown in Fig. 3(b), white mud has a porous structure, which increases the water demand.

### 3.2. Setting time

The setting time of AAWS paste is shown in Fig. 5 and Fig. 6. In general, the setting time is shorter for the water glass activated systems compared to the sodium hydroxide activated systems. The setting time is relevant to the reaction rate influenced by the reactivity of the precursor and the alkalinity of the activator. NaOH is more alkaline than water glass with the same Na<sub>2</sub>O concentration, and it contributes to the dissolution of the vitreous structure of the slag. The amount and distribution of silicate ions in the water glass is more conducive to promote the early reaction, generating gel products and accelerating setting and hardening [41].

The increased white mud amount leads to a shortening of both initial and final setting times, see Fig. 5 and Fig. 6. White mud is strongly alkaline [34]. Replacing GGBFS with white mud corresponds to strengthening the alkali environment, diluting the reactive precursors and therefore accelerating the reaction and reducing the setting time. Besides, particles smaller than 5  $\mu$ m account for about 30% of the white mud which is about 50 % higher than that of GGBFS. These particles can provide nucleation sites for the formation of reaction products and facilitate the reaction [21,23];

### 3.3. Autogenous shrinkage

The autogenous shrinkage of AAWS pastes prepared with different activators and white mud dosage over a period of 168 h are shown in Fig. 7 and Fig. 8. The autogenous shrinkages of all samples increase rapidly in first 24 h and then gradually grow up to 168 h, which is consistent with the results reported in literature [42]. The autogenous shrinkage of AAWS activated by water glass is higher than that of AAWS activated by NaOH. The 168-hour autogenous shrinkage of SS30 is 5806  $\mu$ s, 1.5 times that of SH30. The reason may be that water glass activated system has a higher degree of reaction and generates more hydration

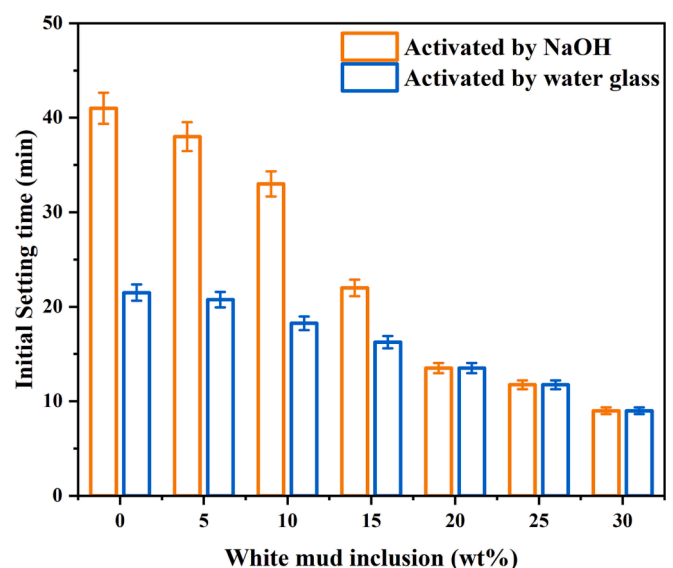


Fig. 5. Initial setting times of AAWS pastes.

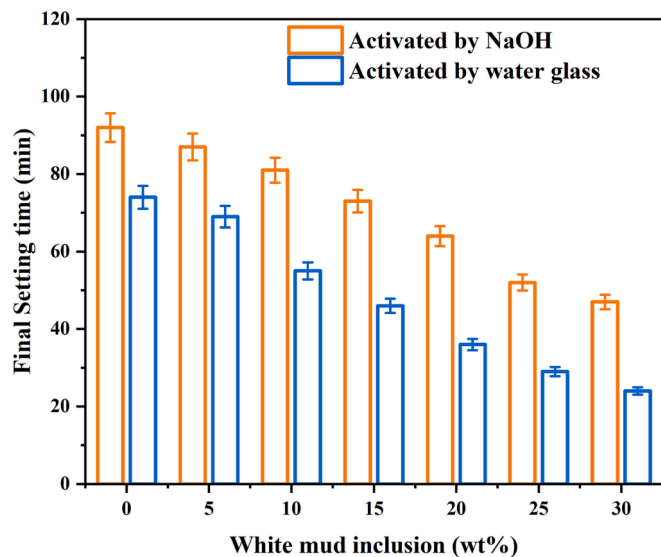


Fig. 6. Final setting times of AAWS pastes.

products. The autogenous shrinkage of AAWS decreases as the inclusion of white mud increases. When 30% white mud is blended, the autogenous shrinkage of AAWS activated by NaOH is reduced by 38% at 168 h. This may be attributed to the restraining effect [43] of the white mud which works as the microaggregate and the reduction of highly reactive GGBS. As shown in Fig. 8, with the incorporation of white mud, the samples shrink faster in the very early stage. This indicates that white mud accelerates the reaction in the early stage, which is consistent with the results of setting time above.

### 3.4. Compressive strength

The compressive strengths of AAWS at different ages (1 day, 7 days, 28 days) are shown in Fig. 9 and Fig. 10. The compressive strength increases faster in the early stage. The strength at 1 day is more than 35 MPa for all mixtures, about 40% of 28d strength. The 7 days compressive strength increases to more than 80% of 28 days strength. The strength increase slows down significantly after 7 days. The compressive strength of the water glass activated samples is higher than those activated by NaOH with the same white mud amount. The compressive strength of SS0 at 1 day, 7 days and 28 days are 49.51 MPa, 94.21 MPa and 114.61

MPa respectively, which are 14.09 MPa, 24.96 MPa and 37.88 MPa higher than that of SH0. For NaOH activated system, GGBFS dissolves  $\text{Ca}^{2+}$ ,  $\text{Si}^{4+}$  and  $\text{Al}^{3+}$  due to the action of  $\text{OH}^-$ . The dissolved ions continue to form gel products. Water glass contains  $\text{Si}^{4+}$ , which allows for a rapid polymerization after the dissolution of  $\text{Ca}^{2+}$ , generating gel products to fill the pores and bond the matrix, resulting in higher compressive strength.

It can be found in Fig. 9 and Fig. 10 that the highest compressive strength is achieved when 15 wt% white mud is blended. The compressive strength of SS15 at 1 day, 7 days and 28 days are 58.15 MPa, 105.48 MPa and 132.36 MPa respectively, which are 8.64 MPa, 11.27 MPa and 17.75 MPa higher than that of SS0. Rashad et al. [44] found the incorporation of 15% limestone powder (LSP) increased the 7 and 28 days compressive strength by an average of 11.41%. In the current study, the incorporation of 15% white mud increases the 7 days compressive strength by 11.96% and increases the 28 days compressive strength by 15.49%, which is 5% and 36% higher than that mentioned in the literature above. The white mud enhances the alkaline environment and a moderate inclusion of white mud dilutes the reactive precursors. Additionally, white mud has a porous structure and a large specific surface area. This facilitates the release of  $\text{Ca}^{2+}$ ,  $\text{Na}^+$ , etc. and those small particles (<5 $\mu\text{m}$ ) provide nucleation sites during the hydration reaction [21], thereby accelerating the pre-reaction rate and improving the mechanical strength. However, there was no obvious difference in terms of strength growth rates of the samples from 7 days to 28 days, indicating that white mud has limited influence at the later stages of the reaction. The compressive strength of SS30 at 1 day, 7 days and 28 days are 47.73 MPa, 84.73 MPa and 93.62 MPa respectively, which are 10.42 MPa, 20.75 MPa and 38.74 MPa lower than that of SS15. The strength is reduced when the percentage of white mud is higher than 15 wt% for the following reasons: 1) The large inclusion of white mud increases the specific surface area of the mixture and increases the water demand, which makes it difficult to mix uniformly and results in particle agglomerations [45]; 2) The dilution effect of excessive white mud reduces the total amount of reaction products in the system, which affects the development and growth of gel products, resulting in a loose microstructure [46]; 3) The white mud particles are poorly bound with the reaction products, becoming the weak spot in the matrix [47].

### 3.5. Chemical composition characterization

#### 3.5.1. XRD

The XRD results of AAWS samples cured for 28 days are shown in Fig. 11 and Fig. 12. The broad hump at  $2\theta = 27$  to  $32^\circ$  represents C-S-H

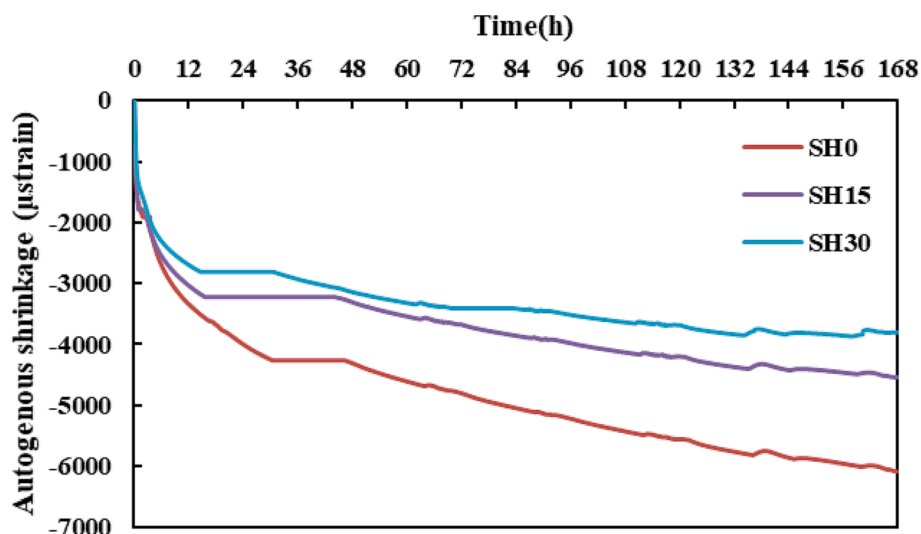


Fig. 7. Autogenous shrinkage of AAWS activated by NaOH.

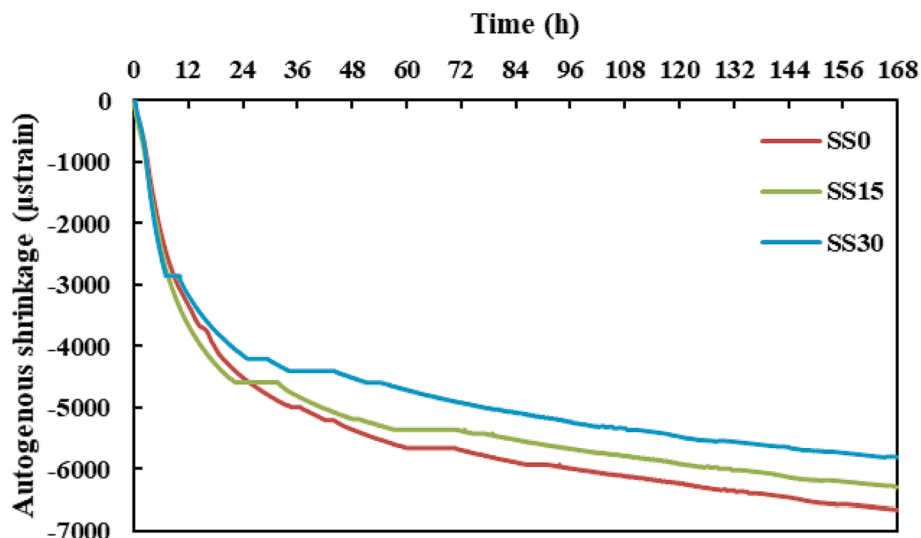


Fig. 8. Autogenous shrinkage of AAWS activated by water glass.

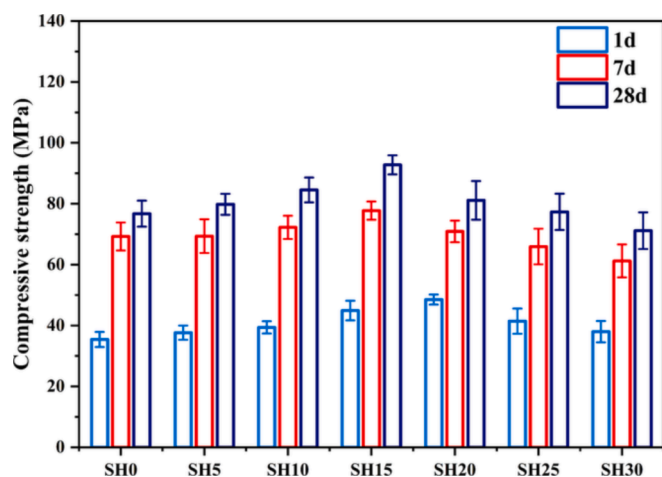


Fig. 9. Compressive strength development of AAWS activated by NaOH.

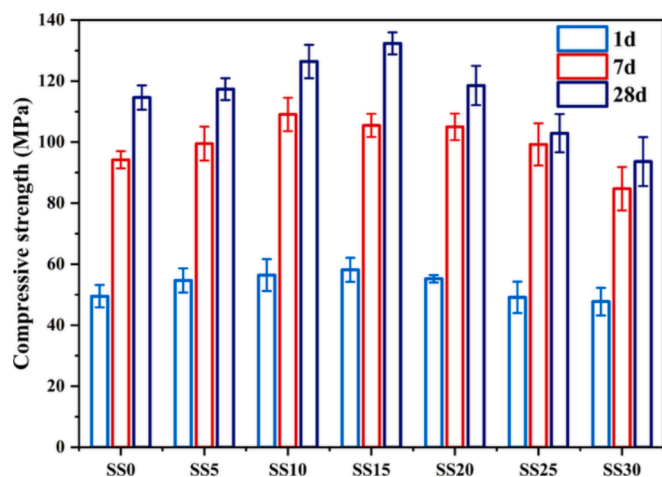


Fig. 10. Compressive strength development of AAWS activated by water glass.

which is generated by the reaction of slag and alkali activator [48–50]. Considering the presence of abundant  $\text{Ca}^{2+}$ ,  $\text{Na}^+$  and  $\text{Al}^{3+}$  in the system, ion exchange may occur to form C-(N)-A-S-H [51]. Diffraction peaks of

calcite appear around  $2\theta = 30^\circ$ ,  $39^\circ$  and  $48^\circ$  in the samples with white mud. The intensity of the diffraction peaks grows with the white mud percentage, indicating a low chemical activity of the white mud. The reaction products of the NaOH activated system include calcite ( $\text{CaCO}_3$ ), hydrotalcite ( $\text{Mg}_6\text{Al}_2(\text{CO}_3)(\text{OH})_{16}\cdot 4\text{H}_2\text{O}$ ), akermanite ( $\text{Ca}_2\text{MgSi}_2\text{O}_7$ ), hatrurite ( $\text{Ca}_3\text{SiO}_5$ ) and vaterite ( $\text{CaCO}_3$ ). The presence of vaterite indicates that carbonation occurred during mixing or maintenance [52]. In the water glass activated system, only calcite and hydrotalcite are observed as the reaction products.

The composition of the GGBFS, the type of activator, the alkali concentration and the maintenance conditions all influence the reaction products of AAS [50]. It has been demonstrated that the presence of different types of calcium crystals can be detected in  $\text{CaCO}_3$  systems activated by water glass, such as pirssonite ( $\text{CaNa}_2(\text{CO}_3)_2\cdot 2\text{H}_2\text{O}$ ) and portlandite ( $\text{Ca}(\text{OH})_2$ ) [53]. Gao et al. [23] found that  $\text{Ca}^{2+}$  was released from the fine limestone particles under alkali activation, then participated in the reaction process. As  $\text{CaCO}_3$  is soluble in NaOH [54],  $\text{Ca}^{2+}$  released from white mud in the NaOH-activated system may be involved in the crystallization reaction of hatrurite ( $\text{Ca}_3\text{SiO}_5$ ). However, none of these products is observed in the water glass system. This suggests that  $\text{Si}^{4+}$  from the water glass restricts the formation of the calcium crystals [55]. Therefore, in the water glass activated system,  $\text{Ca}^{2+}$  from white mud is more likely to undergo condensation reactions with  $\text{Si}^{4+}$  and  $\text{Al}^{2+}$  from the slag to form C-(N)-A-S-H.

The diffraction peaks appearing at  $2\theta = 11.5^\circ$  and  $2\theta = 23^\circ$  represent the existence of hydrotalcite ( $\text{Mg}_6\text{Al}_2(\text{CO}_3)(\text{OH})_{16}\cdot 4\text{H}_2\text{O}$ ) [56] which is a magnesium–aluminum hydroxycarbonate with a layered crystal structure. It has been reported by [57–59] that, in the AAS system, the formation of hydrotalcite happens only when the MgO content is at least 5%. As shown in Table 1, the content of MgO in the slag is about 2.72 wt % and no hydrotalcite phase is found in SS0. This suggests that the  $\text{Mg}^{2+}$  attached to the calcium carbonate in the white mud would be released to the pore solution after exposure to the activator and reacted with the  $\text{Al}^{3+}$  dissolved from the slag to produce hydrotalcite. In addition, it should be noted that the release of  $\text{CO}_3^{2-}$  from  $\text{CaCO}_3$  also contributes to the formation of hydrotalcite [60].

### 3.5.2. FTIR

The FTIR spectra of the GGBFS and white mud are shown in Fig. 13 and the main FTIR vibration bands corresponding to the chemical bonds are shown in Table 3. The peak at  $954\text{ cm}^{-1}$  in the GGBFS spectrum corresponds to the asymmetric stretching vibration of Si-O-T (T = tetrahedral Si or Al) [61]. This broad intense band indicates that the slag is mainly composed of amorphous silica-aluminates [62]. The main

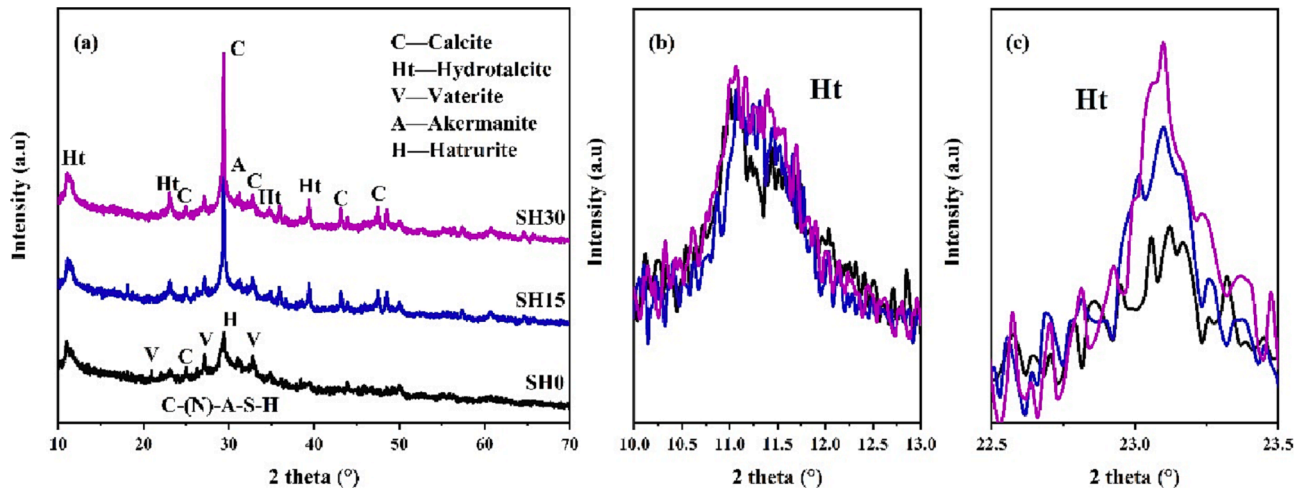


Fig. 11. XRD patterns of (a) NaOH activated AAWS paste. (b) is a zoom between  $2\theta = 10 \sim 13^\circ$  and (c) is a zoom between  $2\theta = 22.5 \sim 23.5^\circ$  (C = Calcite, Ht = Hydrotalcite, V = Vaterite, A = Akermanite, H = Hatrurite).

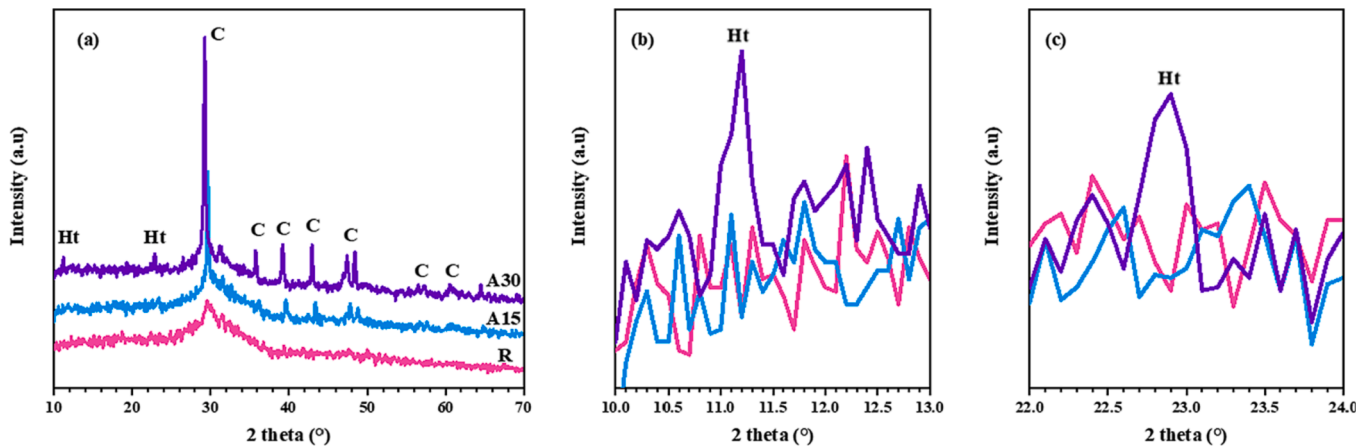


Fig. 12. XRD patterns of (a) water glass activated AAWS paste. (b) is a zoom between  $2\theta = 10.5 \sim 12^\circ$  and (c) is a zoom between  $2\theta = 22.5 \sim 23.5^\circ$  (C = Calcite, Ht = Hydrotalcite).

vibration bands ( $1791\text{ cm}^{-1}$ ,  $1442\text{ cm}^{-1}$ ,  $873\text{ cm}^{-1}$ ,  $712\text{ cm}^{-1}$ ) of white mud follow the asymmetric stretching vibration of C-O-C [63].

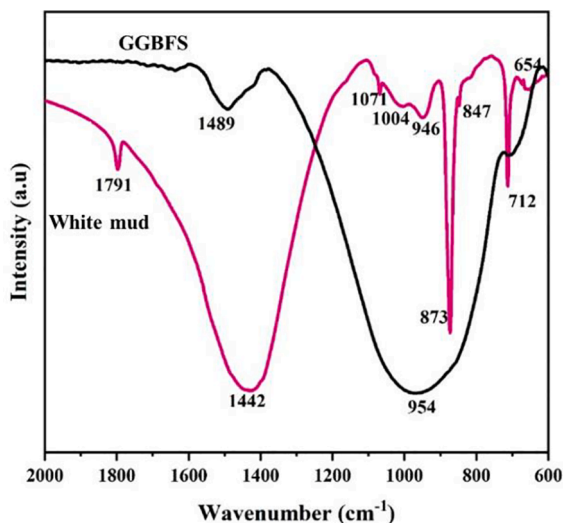


Fig. 13. FTIR spectra of raw materials.

The FTIR spectra of AAWS at the age of 28 days are shown in Fig. 14 (a). The bending vibrational absorption peak of the O-H bond is close to  $1640\text{ cm}^{-1}$ , representing the chemically bound water within the reaction product. As the amount of white mud increases, the relative content of the reaction products decreases, and the peak area of the O-H bond decreases. The disappearance of the absorption peaks at  $1071\text{ cm}^{-1}$ ,  $1004\text{ cm}^{-1}$  and  $847\text{ cm}^{-1}$  in the white mud signifies the involvement of white mud in the reaction. The shift in the absorption peak of the Si-O-T bond at  $954\text{ cm}^{-1}$  in the slag towards higher wave numbers is due to the disruption of the silica-aluminum glass structure within the slag and the polymerization reaction which produces the main hydration product, e. g., silica-alumina gels.

The variation of Si-O-T bond wave number for samples cured for 1, 7 and 28 days are shown in Fig. 14(b). The wave number of the specimens activated by water glass is higher than that activated by NaOH due to the higher content of silicate ions in the water glass, which facilitates the

Table 3

FTIR vibrational bands of AAWS corresponding to chemical bonds.

Wavenumber ( $\text{cm}^{-1}$ )	Chemical bond
654	Mg-O
712, 873, 1424, 1486, 1798	C-O ( $\text{CO}_3^{2-}$ )
950 ~ 1020	Si-O-T (T = Si, Al)
1648	O-H

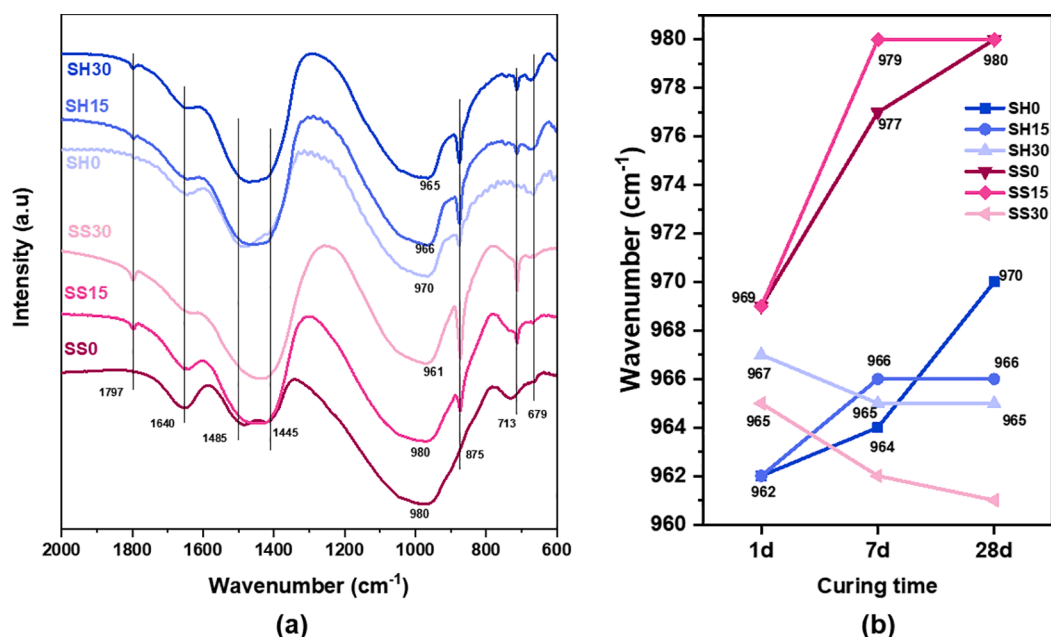


Fig. 14. FTIR spectra of AAWS mixtures: (a) typical mixtures cured for 28 days, (b) Si-O-T bands of typical mixtures during 1 and 28 days.

polymerization of the gel network. The wave number of this Si-O-T bond is related to the Al/Si and Ca/Si ratios. A higher wave number suggests a higher degree of polymerization of the Si-O-T chains. The dissolution rate of elements within the slag is related to the bonding energy of the chemical bonds. Ca-O and Al-O have weak bonding energies and therefore faster dissolution rates. Si-O has stronger bonding energy leading to a slower dissolution rate. In the early stage of the reaction, low polymerization gel products with high Ca/Si and Al/Si ratios are easily formed in the system. In the later stage of the reaction, the dissolution of Si rises, some of the Al in the gel structure is replaced by Si, and the degree of polymerization increases. Therefore, the wave number of Si-O-T bonds in AAS tends to reduce and then improve with age [51,64,65]. As shown in Fig. 14(b), the Si-O-T bond wave number of SS0 and SH0 gradually increases with the age, while the Si-O-T bond wave number of SS15 and SH15 keeps increasing until 7 days and then remains stable. Conversely, the Si-O-T bond wave number of SS30 and SH30 reduced with the age. When 15 wt% white mud was mixed, the reaction was accelerated, and a large amount of Al dissolved within 1 day. Therefore, no obvious change in the wave number of the Si-O-T bond could be detected after 7 days. The opposite trend observed for SH30 and SS30 is attributed to the fact that the excess white mud is attached to the slag particle surface and impedes the dissolution of Si and Al. Besides, the white mud enhanced the Ca/Si in the gel structure, resulting in a lower wave number of the Si-O-T bond.

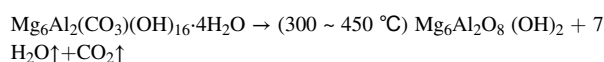
The peak at 670 cm<sup>-1</sup> corresponds to the bending vibration of the Mg-O bond, which evolves from 654 cm<sup>-1</sup> in the white mud, indicating the presence of hydrotalcite. It grows with white mud and is more pronounced in the spectrum of the NaOH activated system, which is related to its higher hydrotalcite content. This is consistent with the observation from XRD measurements. In addition, there are vibration bands at 875 cm<sup>-1</sup> in the spectrum of SH0 and two overlapping bands between 1500 cm<sup>-1</sup> and 1420 cm<sup>-1</sup> in the spectrum of SS0, which correspond to the tensile vibration of O-C-O in carbonates. This shows that the specimens have undergone slight carbonation during mixing or curing. The appearance of absorption zones at 713 cm<sup>-1</sup>, 875 cm<sup>-1</sup> and 1797 cm<sup>-1</sup> is attributed to the presence of CaCO<sub>3</sub> in the white mud [66]. The area of the O-C-O absorption bands (712 cm<sup>-1</sup>, 873 cm<sup>-1</sup>, 1430 cm<sup>-1</sup> and 1798 cm<sup>-1</sup>) rises with white mud addition, demonstrating that a substantial amount of CaCO<sub>3</sub> remains in the system.

### 3.5.3. TGA

The results of the thermogravimetric analysis are shown in Fig. 15. The mass loss of the water glass activated system is higher for the same white mud inclusion. The mass loss fraction for SS15 is 10.6% higher than that of SH15. The maximum test temperature is lower than the decomposition temperature of slag (above 1200 °C). Therefore, it can be concluded that the water glass activated system is more reactive, which is consistent with the above analysis.

Four peaks are present in the mass loss rate plots for all investigated mixtures. The first weight loss peak appears in 30–250 °C. This is caused by the evaporation of bound water (30–105 °C) and crystalline water, and the decomposition of the gel products (105–250 °C) [67]. This peak for the NaOH activated system is centered at 105 °C, while that for the water glass activated system is centered at higher temperature, suggesting that a more stable gel structure is generated. Furthermore, the peak areas of SS0 and SS15 are larger than in other mixtures, demonstrating a higher gel content. The significant reduction of the peak area in SS30 tends to confirm the aforementioned assumption that the excess white mud impedes the dissolution of Si and Al in slag which reduces the amount of gel products.

The second weight loss peak that occurs between 300 and 450 °C generally improves with white mud. It corresponds to the decomposition of hydrotalcite. Specifically, the evaporation of interlayer bound water and CO<sub>2</sub> at 300 °C leads to the complete decomposition of the layered structure at 450 °C with the following chemical expressions [60,68,69].



Two distinct peaks appear when the temperature exceeds 500 °C. This indicates not only the decomposition of carbonates, including sodium, magnesium and calcium carbonate, but also the decomposition of silica gel [70,71]. Insignificant peak is found for SS0 and SH0 above 500 °C. In this temperature range, the weight loss increases with the incorporation of white mud, especially for the water-glass activated system. The sharp heat absorption peak at 700–750 °C represents the complete decomposition of calcium carbonate [72]. This weight loss peak in SH0 reflects a certain degree of carbonation of the sample. The intensity of this weight loss peak correlates with the white mud addition, showing that some of the calcium carbonate from the white mud is still stable in the matrix and does not participate in the reaction. All samples

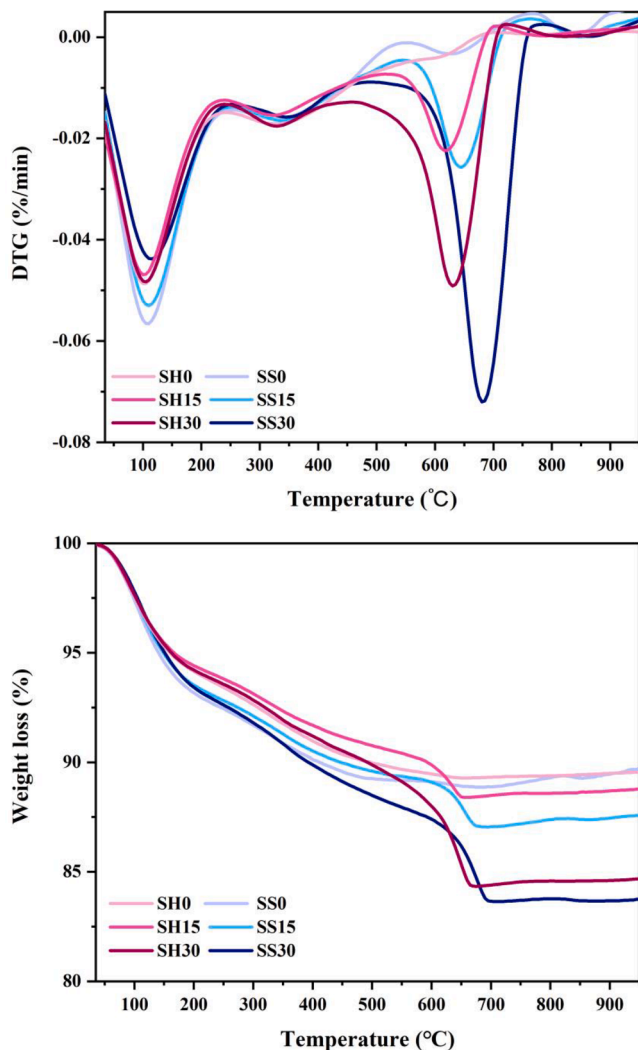


Fig. 15. TGA analysis for AAWs pastes with different white mud inclusion and alkali activator after 28 days curing (a) DTG analysis, (b) TG analysis.

showed several exothermic peaks after 800 °C, but there is no significant difference in mass loss rate, indicating that the type of activator and the amount of white mud almost have no influence on the peaks in this range. According to existing studies [73], new phases are generated at 800 °C. C-A-S-H gels completely lose their bound water and the disrupted gel structure begins to form more ordered crystalline phases, such as akermanite.

Assuming that the decomposition peaks in different intervals refer to the content of gel (105 ~ 250°C), hydrotalcite (300 ~ 450°C) and white mud (450 ~ 750°C) in the system, the mass loss rate of each sample is recorded, and the results are shown in Table 4. As can be seen from the table, the white mud has an important effect on the hydration reaction of the system. The appropriate amount of white mud can improve the overall reaction degree of the system with the promotion of hydrotalcite production.

### 3.5.4. SEM images

Figs. 16-21 show the microstructure and gel product morphology of the AAWs with different white mud contents. It can be found that the glass phase of the slag particles reacts and generates a substantial amount of gel. These gels are in the form of random network and amorphous globular structure, which grow interlocked with each other, accumulate around the unreacted particles, and fill the voids. The incompletely reacted slag particles with rough and well-defined angular

Table 4

Mass loss rate of the AAWs at different temperature intervals (%).

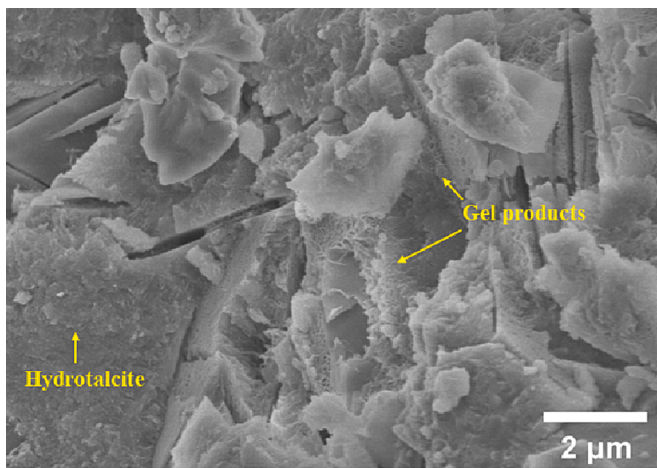
Code	Temperature interval			
	105 ~ 250 °C	300 ~ 450 °C	450 ~ 600 °C	600 ~ 750 °C
SH0	3.81	1.96	0.89	0.06
SH15	3.88	2.27	1.29	1.30
SH30	3.54	2.32	2.52	3.47
SS0	4.63	2.11	0.46	0.11
SS15	4.88	2.15	0.89	1.90
SS30	4.19	2.69	1.72	3.71

surfaces can also be observed. This is related to the reaction kinetics of the AAS. At the beginning of the reaction, layers rich in Si and Al are easily formed in the surface of the slag particles, and at a later stage, the dissolution of  $Mg^{2+}$  leads to the formation of slab-like hydrotalcite [57]. Hydrotalcite is a kind of layered double hydroxide, in both composition and structure [74]. It can be observed that layered and lamellar crystals staggered together with gel products in SE images. The white mud particles are disorderly dispersed and accumulated everywhere. The space is mainly composed of gel products, hydrotalcite, slag and white mud particles, and the other crystalline products in the NaOH system are not accurately identified due to scale limitations.

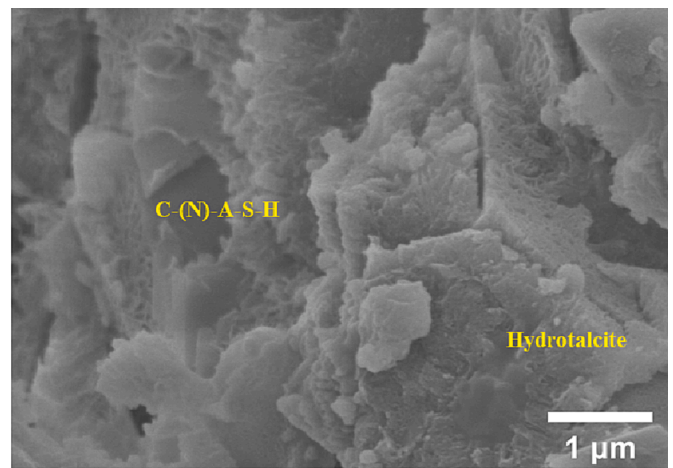
As can be seen in Fig. 16(a), the surface of the slag particles is wrapped in a fibrous C-(N)-A-S-H gel and lamellar hydrotalcite after the reaction in the NaOH system. The gel structure is loose and the hydrotalcite is interspersed and interlaced with the gel products. However, Fig. 16(b) shows that there are still numerous cracks and micropores within the microstructure. In Fig. 17, the amorphous gel product is transformed into a lamella structure when 15% of white mud is incorporated. The generation and development of hydrotalcite is promoted and the layer thickness increases. In addition, the gel network structure becomes denser and the porosity is reduced, indicating a higher degree of reactivity. It corresponds to the enhanced mechanical properties of SH15. Less reaction products within the matrix can be observed in Fig. 18, suggesting that the excessive white mud hinders the reaction.

Compared with the NaOH activated system, the gel structure of the water glass activated systems is denser, see Figs. 19-21. However, some evident pores and defects in the microstructure of SS0 can be observed in Fig. 19. With the incorporation of 15 wt% white mud, the angular slag particles are no longer visible in Fig. 20 because more slag is involved in the hydration reaction to form silica-aluminate gel. The gel and white mud particles completely encase the slag and form a continuous unity, resulting in a denser microstructure. The higher degree of reactivity of SH15 and SS15 is consistent with the above analysis, while the denser microstructure corresponds to the better macroscopic mechanical strength. As shown in Fig. 21, the excessive white mud particles found in SS30 restrict the growth of the gel products. The continuity of the microstructure is poor and there are more microscopic defects, thus the specimen exhibits lower mechanical properties.

The microstructure of the water glass activated system is denser than that of the NaOH activated system. The presence of reactive Si in the water glass solution improves the degree of polymerization of the gel structure. The microstructure of the gel products with no white mud is more compact, indicating a relatively high degree of polymerization. Minor defects appear in the gel structure when 15 wt% white mud is added, as can be seen in Fig. 16 and Fig. 19. More defects appear with the increment of white mud content, see Fig. 17. Possible explanations are as follows: 1) release of  $Ca^{2+}$  from  $CaCO_3$  in white mud and diffusion of  $Na^+$ ,  $Mg^{2+}$  and  $K^+$  carried by white mud into the pore solution promotes the hydration reaction. 2) The excessive white mud is attached to the surface of the slag particles and inhibits the dissolution of Si and Al. The concentration of ions to form the gel structure ( $Si^{4+}$ ,  $Al^{3+}$ ) drops, and the number of bonds with large radius and low bond energy in the gel structure increases, which ultimately reduces the degree of polymerization. This corresponds to the reduced mechanical properties and

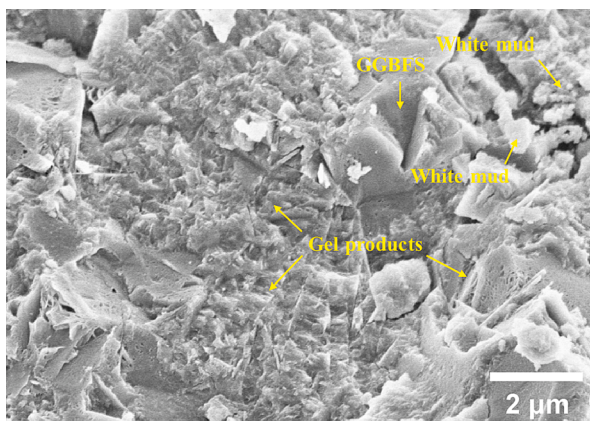


(a)

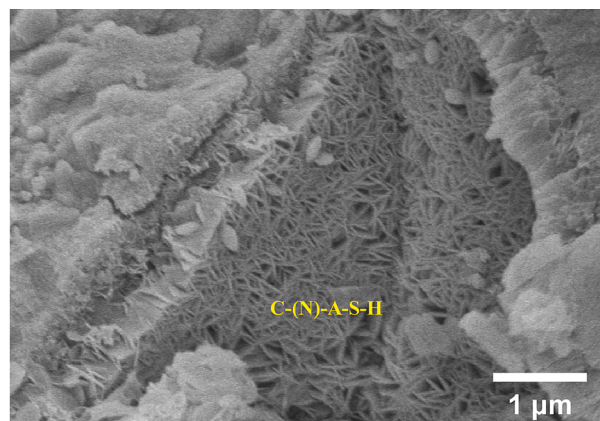


(b)

Fig. 16. SEM micrographs of (a) microstructure in SH0 and (b) is a partial enlarged detail of gel products.

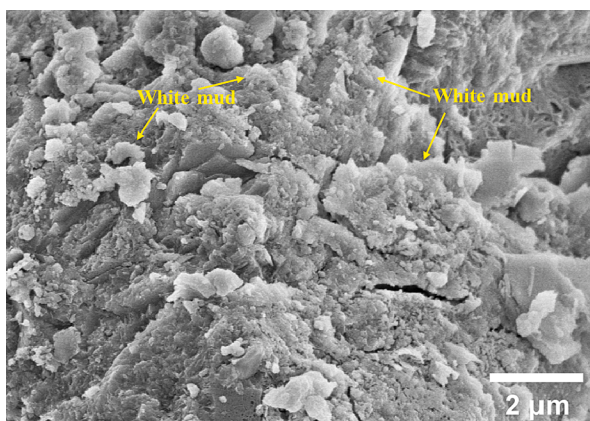


(a)

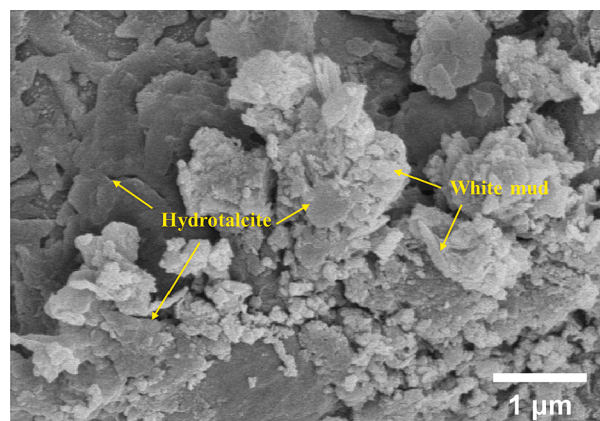


(b)

Fig. 17. SEM micrographs of (a) microstructure in SH15 and (b) is a partial enlarged detail of gel products.



(a)



(b)

Fig. 18. SEM micrographs of (a) microstructure in SH30 and (b) is a partial enlarged detail of gel products.

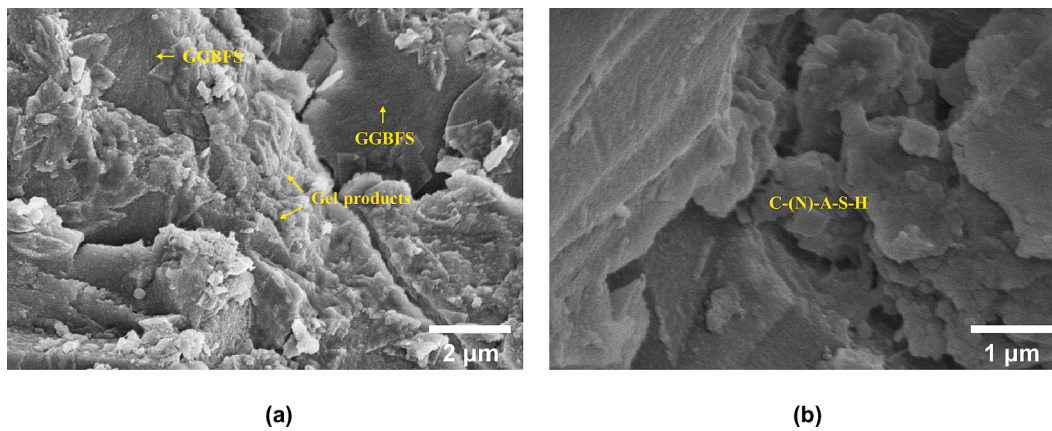


Fig. 19. SEM micrographs of (a) microstructure in SS0 and (b) is a partial enlarged detail of gel products.

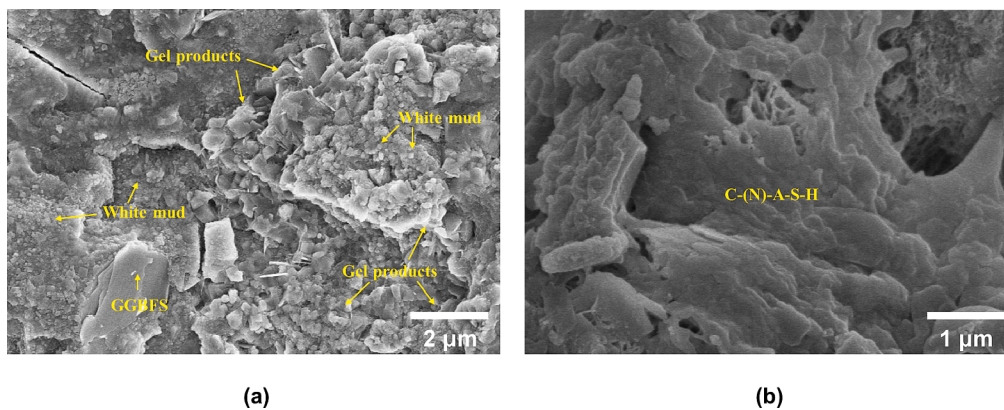


Fig. 20. SEM micrographs of (a) microstructure in SS15 and (b) is a partial enlarged detail of gel products.

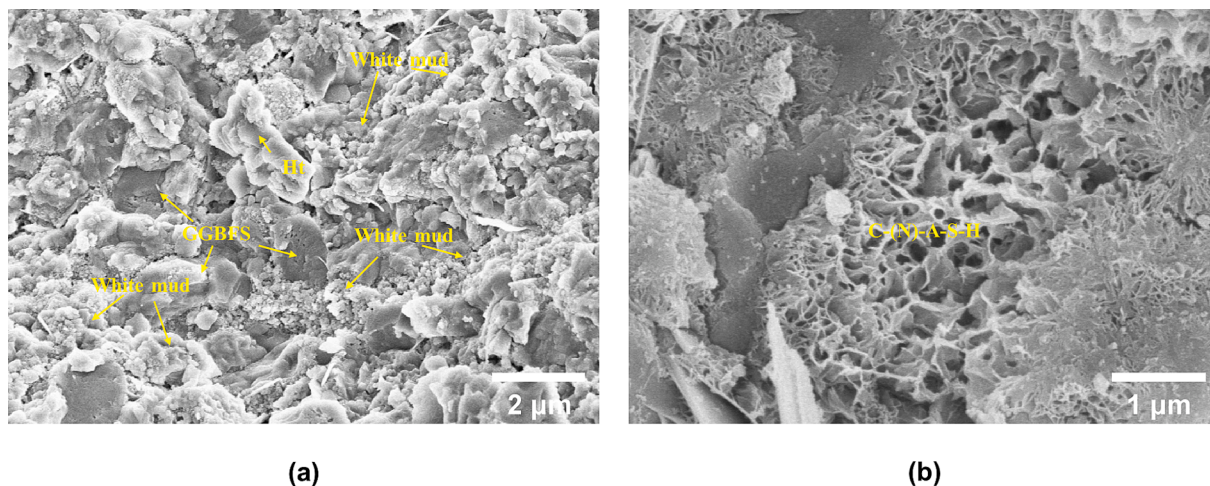


Fig. 21. SEM micrographs of (a) microstructure in SS30 and (b) is a partial enlarged detail of gel products.

the lower vibrational wave number of the Si-O-T bond.

### 3.5.5. BSE-EDS

The elemental distribution of SS0 and SS30 was analyzed by EDS line scan, see Fig. 22 and Fig. 23. There exists a dark rim that separates the GGBFS particles from the gel products. The dark rim has higher relative contents of Mg and Al than C-A-S-H and unhydrated GGBFS, while it has lower relative contents of Ca and Si. This is similar to the cement/slag system [75]. The presence of the dark rim is related to the enrichment of

Mg in the outer layer of GGBFS and the formation of layered double hydroxide (LDH) during the hydration process of GGBFS. The most abundant element in the region of the gel products of SS0 and SS30 is Si followed by Ca and Al. The content of Si is more than 50%, which is determined by the structural characteristics of the amorphous C-(N)-A-S-H gel. The content of Al in the slag is lower than that of Mg, indicating that most of the Al has been dissolved and diffused into the pore solution to participate in the reaction. When the white mud is mixed, the content of Ca and Na increase in the gel region near the white mud particles. This

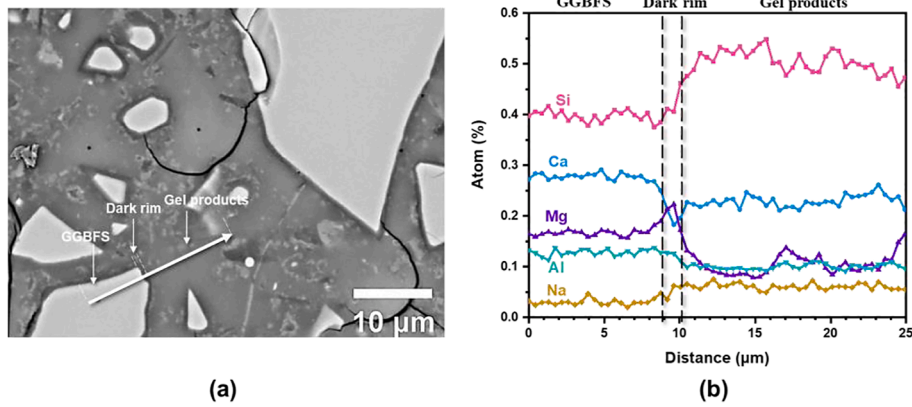


Fig. 22. Line analysis of GGBFS particle in SS0 mixture curing for 28 days.

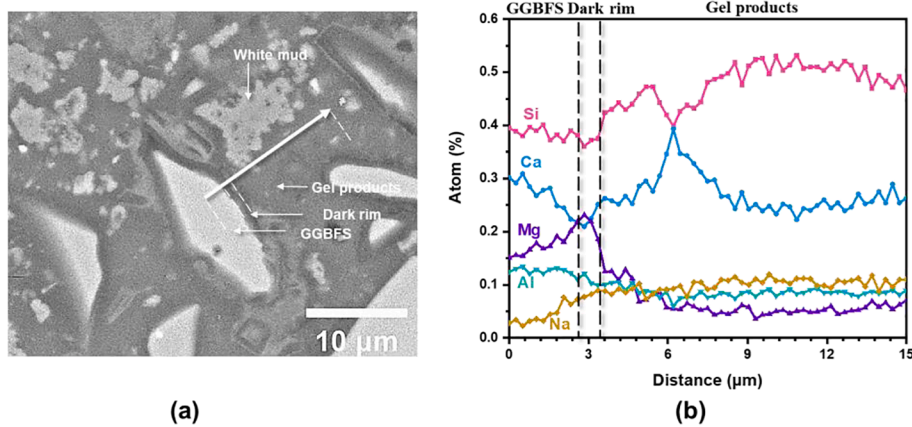


Fig. 23. Line analysis of GGBFS particle in SS30 mixture curing for 28 days.

suggests that white mud dissolves Ca and Na and they are involved in the production of C-(N)-A-S-H gels, which is consistent with the results obtained in the above SEM analysis. It is noted that the content of Mg decreases in the region near the white mud, while the relative content of Mg in the dark rim increases when white mud is blended. Therefore, Mg dissolved from the white mud may migrate to the dark rim to form LDH.

Point scans of the gel products in the SH0, SH30, SS0 and SS30 specimens are carried out using Energy Dispersive Spectroscopy (EDS) respectively. The ratios of Ca, Si and Al are normalized and plotted in a ternary diagram as shown in Fig. 24. The different dashed areas in this ternary diagram reflect the Ca/(Si + Al) ratio for C-A-S-H, C-(N)-A-S-H and N-A-S-H [76–78]. Fig. 25.

The test results show that the main gel products in the AAWS with different white mud admixtures all fall in the same region. The results above show that the main reaction product in the AAWS system is the C-(N)-A-S-H gel, where Na<sup>+</sup> balances the negative ions. The Ca and Na released from white mud are also involved in the condensation reaction, replacing Al and Si, resulting in an increased Ca/(Si + Al) ratio. It should be noted that, due to the limited resolution of the current EDS technique, the depth acting on the specimen surface is about 1.0–2.5 μm at an accelerating voltage of 15 kV, the possibility of the coexistence of C-(N)-A-S-H/ (N, C)-A-S-H gel cannot be excluded.

The Ca/Si and Si/Al ratios of the C-(N)-A-S-H play a crucial role in the mechanical properties of the AAWS. The water-glass introduces active Si into the system to further participate in the polymerization reaction. Besides, some of the Al is consumed during the formation of the hydrotalcite phase in the NaOH activated system. Therefore, the Si/Al of the gels in the water-glass activated system is higher, resulting in higher compressive strength.

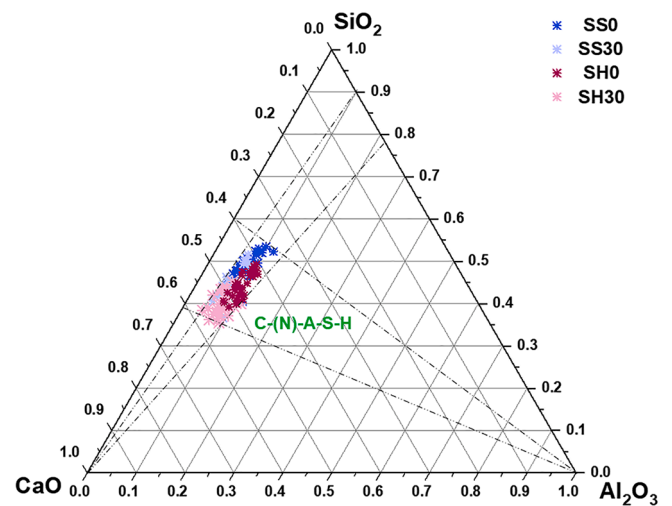


Fig. 24. Ternary diagram of EDX spot analysis of AAWS paste mixtures cured for 28 days.

### 3.5.6. Discussion

According to the model proposed by Jia et al. [57], the formation process of products in the AAS system consists of the following three main stages.

Stage 1: When alkaline activator is blended with GGBFS, the outer layer of GGBFS will dissolve Ca<sup>2+</sup>, Si<sup>4+</sup> and Al<sup>3+</sup> rapidly due to the action of OH<sup>-</sup>. The surface of a GGBFS particle provides a nucleation site

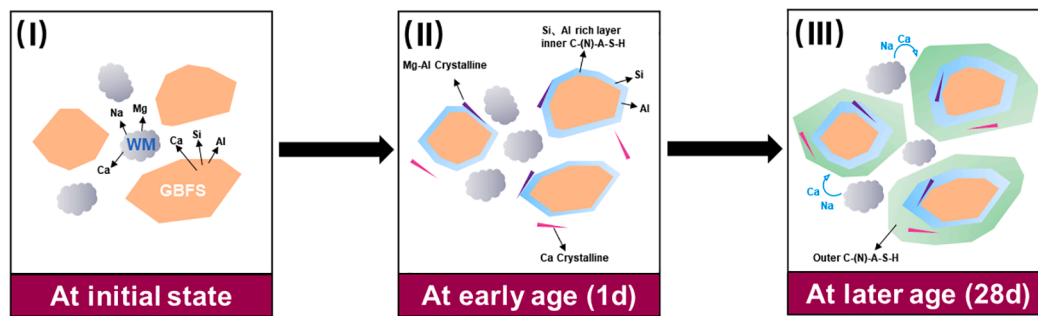


Fig. 25. Formation processes of reaction products and microstructure in AAWS system.

for the hydration products and a layer of C-A-S-H gel will be formed immediately around the GGBFS particle due to the relatively fast initial reaction rate.

Stage 2: As shown in Fig. 22, when the surface of the GGBFS particle is completely covered by C-A-S-H gel, the dark rim starts to be formed in the outer layer of the GGBFS particle. Ca, Si, Al and Mg begin to dissolve from the outer layer of the GGBFS. The dissolved ions continue to form new C-A-S-H gel and increase the layer thickness. The dissolution rate of Ca and Si is the highest while the dissolution rate of Mg is the lowest. Therefore, the gel products are relatively high in Ca and Si. When  $\text{Na}^+$  and  $\text{OH}^-$  from the solution diffuse through C-A-S-H gel into the outer layer of GGBFS, they react with the remaining Ca, Si, Mg and Al to form C-(N)-A-S-H gel. At the same time,  $\text{OH}^-$  will react with Al and Mg to form hydrotalcite, which is wrapped inside and mixed with the gel products to form a composite phase.

Stage 3: With elapsed time, the reaction within the slag continues, and the thickness of the dark rim increases.

In the first stage of the reaction,  $\text{Ca}^{2+}$ ,  $\text{Na}^+$ ,  $\text{Mg}^{2+}$  released by white mud are free in the liquid environment and participate in the reaction. This reduces the setting time. Excessive addition of white mud causes the matrix to set and harden rapidly, and limits the diffusion of Si and Al during the second stage of the reaction. This leads to a reduced gel content. Furthermore, it results in the migration of  $\text{Ca}^{2+}$  and  $\text{Na}^+$  due to charge balance, and eventually decreases the degree of polymerization. As it has been shown by the XRD, the NaOH activated system has more types of hydration products than the water-glass activated system, including hydrotalcite ( $\text{Mg}_6\text{Al}_2(\text{CO}_3)(\text{OH})_{16}\cdot 4\text{H}_2\text{O}$ ) and hatrurite ( $\text{Ca}_3\text{SiO}_5$ ). This can be attributed to the higher alkalinity of the NaOH solution, which facilitates the dissolution of Ca, Si, Al and Mg from the slag to participate in the reaction during the first stage.

#### 4. Conclusions

In this study, the physical and mechanical properties including fluidity, setting time and compressive strength of AAWS were tested, the hydration products and microstructure were characterized by XRD, FTIR, TGA and SEM-EDS. The mechanism of white mud on the hydration process of AAS was explored to explain the development of macroscopic properties. The main conclusions are as follows:

- The incorporation of white mud reduces the fluidity, setting time and autogenous shrinkage of the AAS. The compressive strength of AAS with white mud addition is improved when the inclusion was below 15 wt%. When 15 wt% of white mud is blended, the 1d, 7d and 28 days strengths of the NaOH activated system increase by 26.82%, 12.27% and 20.92% respectively. The 1d, 7d and 28 days strengths of the water glass activated system increase by 17.45%, 11.96% and 15.48% respectively.
- The main gel product in the AAWS with different white mud admixtures is C-(N)-A-S-H gel. The  $\text{Ca}^{2+}$  and  $\text{Na}^+$  in white mud can participate in the polymerization reaction to produce gels. As the

content of white mud is increased, the  $\text{Ca}/(\text{Si} + \text{Al})$  ratio of the gel increases, and the degree of polymerization of the gel structure is reduced.

- The water glass activated system has a denser microstructure than the NaOH activated system. When 15% of white mud is used, a higher hydration degree is reached. The amorphous gel product is transformed into a lamellar structure and the formation of hydrotalcite is promoted. Excessive white mud limits the dissolution of Si and Al, thus impeding the hydration reaction.
- The NaOH activated system contains more types of hydration products than the water glass activated system, including hydrotalcite ( $\text{Mg}_6\text{Al}_2(\text{CO}_3)(\text{OH})_{16}\cdot 4\text{H}_2\text{O}$ ) and hatrurite ( $\text{Ca}_3\text{SiO}_5$ ). White mud can provide  $\text{Mg}^{2+}$ ,  $\text{CO}_3^{2-}$ , which promotes Mg-Al precipitation and the formation of hydrotalcite.  $\text{Mg}^{2+}$  dissolved from the white mud may migrate to the dark rim.

White mud has potential reactivity and can partially replace slag to prepare new alkali activated materials. Future research is required on the influences of white mud on other properties, e.g., durability of the materials.

#### CRediT authorship contribution statement

**Renjuan Sun:** Methodology, Supervision, Writing – review & editing. **Linglai Bu:** Investigation, Writing – original draft. **Hongzhi Zhang:** Supervision, Writing – review & editing. **Yanhua Guan:** Writing – review & editing. **Chuanyi Ma:** Funding acquisition, Supervision. **Zhi Ge:** Methodology, Supervision. **Branko Savija:** Methodology, Writing – review & editing.

#### Declaration of Competing Interest

The authors declare that they have no known competing financial interests or personal relationships that could have appeared to influence the work reported in this paper.

#### Data availability

Data will be made available on request.

#### Acknowledgements

This work was supported by 111 Project (No. B21012), the Key Basic Research Project of China (No. 2022YFC3005604), Taishan Scholars Foundation of Shandong Province (No. tsqn201909032) and Natural Science Foundation of Shandong Province (No. ZR2021ME215).

#### References

- [1] P.J.M. Monteiro, S.A. Miller, A. Horvath, Towards sustainable concrete, *Nat. Mater.* 16 (7) (2017) 698–699.

- [2] O.F. Arbelaez Perez, D.R. Florez, L.M. Zapata Vergara, K.V. Hernández Benavides, Innovative use of agro-waste cane bagasse ash and waste glass as cement replacement for green concrete. Cost analysis and carbon dioxide emissions, *J. Clean. Prod.* 379 (2022), 134822.
- [3] A. Saludung, T. Azeyanagi, Y. Ogawa, K. Kawai, Effect of silica fume on efflorescence formation and alkali leaching of alkali-activated slag, *J. Clean. Prod.* 315 (2021), 128210.
- [4] P. Chen, Z. Shi, S. Cao, P. Liu, X. Rong, L. Wang, Mechanical properties of alkali-activated slag lightweight aggregate concrete, *J. Clean. Prod.* 359 (2022), 132136.
- [5] J.L. Provis, Alkali-activated materials, *Cem. Concr. Res.* 114 (2018) 40–48.
- [6] K. Arbi, M. Nedeljković, Y. Zuo, G. Ye, A Review on the Durability of Alkali-Activated Fly Ash/Slag Systems: Advances, Issues, and Perspectives, *Ind. Eng. Chem. Res.* 55 (19) (2016) 5439–5453.
- [7] P. Zhang, Z. Gao, J. Wang, J. Guo, S. Hu, Y. Ling, Properties of fresh and hardened fly ash/slag based geopolymer concrete: A review, *J. Clean. Prod.* 270 (2020) 122389.
- [8] C. Lu, Z. Zhang, J. Hu, QijunYu, C. Shi, Effects of anionic species of activators on the rheological properties and early gel characteristics of alkali-activated slag paste, *Cem. Concr. Res.* 162 (2022) 106968.
- [9] Y. Sun, L.M. de Lima, L. Rossi, D. Jiao, Z. Li, G. Ye, G. De Schutter, Interpretation of the early stiffening process in alkali-activated slag pastes, *Cem. Concr. Res.* 167 (2023), 107118.
- [10] V. Trincal, S. Multon, V. Benavent, H. Lahalle, B. Balsamo, A. Caron, R. Bucher, L. Diaz Caselles, M. Cyr, Shrinkage mitigation of metakaolin-based geopolymer activated by sodium silicate solution, *Cem. Concr. Res.* 162 (2022), 106993.
- [11] S. Shi, H. Li, Q. Zhou, H. Zhang, P.A.M. Basheer, Y. Bai, Alkali-activated fly ash cured with pulsed microwave and thermal oven: A comparison of reaction products, microstructure and compressive strength, *Cem. Concr. Res.* 166 (2023), 107104.
- [12] Y. Zheng, F. Rao, L. Yang, S. Zhong, Comparison of ternary and dual combined waste-derived alkali activators on the durability of volcanic ash-based geopolymers, *Cem. Concr. Compos.* 136 (2023), 104886.
- [13] S. Sbi, A. Aboulayt, W. Borja, S. Mansouri, H. El Boudour El, Y. Idrissi, N. Samih, H. Semlal, Y. Hannache, J.A. Tamraoui, An advance understanding of the alkali activation of cover layers waste rocks from phosphate mines: Mechanical, structure and microstructure studies, *Constr. Build. Mater.* 346 (2022), 128472.
- [14] L.B. Oliveira, M.T. Marvila, R. Fediuk, C.M.F. Vieira, A.R.G. Azevedo, Development of a complementary precursor based on flue gas desulfurization (FGD) for geopolymeric pastes produced with metakaolin, *J. Mater. Res. Technol.* 22 (2023) 3489–3501.
- [15] J. He, Y. Jie, J. Zhang, Y. Yu, G. Zhang, Synthesis and characterization of red mud and rice husk ash-based geopolymer composites, *Cem. Concr. Compos.* 37 (2013) 108–118.
- [16] G. Ascensão, M.P. Seabra, J.B. Aguiar, J.A. Labrincha, Red mud-based geopolymers with tailored alkali diffusion properties and pH buffering ability, *J. Clean. Prod.* 148 (2017) 23–30.
- [17] C. Shi, K. Zheng, A review on the use of waste glasses in the production of cement and concrete, *Resour. Conserv. Recycl.* 52 (2) (2007) 234–247.
- [18] H. Zhang, B. Savija, S.C. Figueiredo, E. Schlangen, Experimentally validated multi-scale modelling scheme of deformation and fracture of cement paste, *Cem. Concr. Res.* 102 (2017) 175–186.
- [19] S. Hu, L. Zhong, X. Yang, H. Bai, B.o. Ren, Y. Zhao, W. Zhang, X. Ju, H. Wen, S. Mao, R. Tao, C. Li, Synthesis of rare earth tailing-based geopolymer for efficiently immobilizing heavy metals, *Constr. Build. Mater.* 254 (2020) 119273.
- [20] X. Gao, B. Yuan, Q.L. Yu, H.J.H. Brouwers, Characterization and application of municipal solid waste incineration (MSWI) bottom ash and waste granite powder in alkali activated slag, *J. Clean. Prod.* 164 (2017) 410–419.
- [21] N.R. Rakhimova, R.Z. Rakhimov, N.I. Naumkina, A.F. Khuzin, Y.N. Osin, Influence of limestone content, fineness, and composition on the properties and microstructure of alkali-activated slag cement, *Cem. Concr. Compos.* 72 (2016) 268–274.
- [22] A.A. Adewumi, M.A.M. Ariffin, M.O. Yusuf, M. Masleuddin, M. Ismail, Effect of sodium hydroxide concentration on strength and microstructure of alkali-activated natural pozzolan and limestone powder mortar, *Constr. Build. Mater.* 271 (2021) 121530.
- [23] X. Gao, Q.L. Yu, H.J.H. Brouwers, Properties of alkali activated slag–fly ash blends with limestone addition, *Cem. Concr. Compos.* 59 (2015) 119–128.
- [24] D. Jiang, C. Shi, Z. Zhang, Recent progress in understanding setting and hardening of alkali-activated slag (AAS) materials, *Cem. Concr. Compos.* 134 (2022), 104795.
- [25] W.-J. Long, Z. Wu, K.H. Khayat, J. Wei, B. Dong, F. Xing, J. Zhang, Design, dynamic performance and ecological efficiency of fiber-reinforced mortars with different binder systems: Ordinary Portland cement, limestone calcined clay cement and alkali-activated slag, *J. Clean. Prod.* 337 (2022), 130478.
- [26] J. Xiang, L. Liu, X. Cui, Y. He, G. Zheng, C. Shi, Effect of limestone on rheological, shrinkage and mechanical properties of alkali – Activated slag/fly ash grouting materials, *Constr. Build. Mater.* 191 (2018) 1285–1292.
- [27] Z. Chen, H. Ye, Influence of metakaolin and limestone on chloride binding of slag activated by mixed magnesium oxide and sodium hydroxide, *Cem. Concr. Compos.* 127 (2022), 104397.
- [28] M. Najimi, N. Ghafoori, Engineering properties of natural pozzolan/slag based alkali-activated concrete, *Constr. Build. Mater.* 208 (2019) 46–62.
- [29] H. Egodagamage, H.D. Yapa, H.A.D. Samith Buddika, S. Navaratnam, K. Nguyen, Effective use of biochar as an additive for alkali-activated slag mortar production, *Constr. Build. Mater.* 370 (2023), 130487.
- [30] Z. Li, M. Nedeljković, B. Chen, G. Ye, Mitigating the autogenous shrinkage of alkali-activated slag by metakaolin, *Cem. Concr. Res.* 122 (2019) 30–41.
- [31] B. Yuan, Q.L. Yu, E. Dainese, H.J.H. Brouwers, Autogenous and drying shrinkage of sodium carbonate activated slag altered by limestone powder incorporation, *Constr. Build. Mater.* 153 (2017) 459–468.
- [32] X. Dai, S. Aydin, M. Yücel Yardımcı, R.E.N. Qiang, K. Lesage, G. De Schutter, Rheology, early-age hydration and microstructure of alkali-activated GGBFS-Fly ash-limestone mixtures, *Cem. Concr. Compos.* 124 (2021) 104244.
- [33] A.T.M. Marsh, Z. Yue, Y. Dhandapani, K. Button, S. Adu-Amankwah, S.A. Bernal, Influence of limestone addition on sodium sulphate activated blast furnace slag cements, *Constr. Build. Mater.* 360 (2022), 129527.
- [34] J. Zhang, Q. Wang, J. Jiang, Lime mud from paper-making process addition to food waste synergistically enhances hydrogen fermentation performance, *Int. J. Hydrogen Energy* 38 (6) (2013) 2738–2745.
- [35] J. Cheng, J. Zhou, J. Liu, X. Cao, K. Cen, Physicochemical Characterizations and Desulfurization Properties in Coal Combustion of Three Calcium and Sodium Industrial Wastes, *Energy Fuel* 23 (5) (2009) 2506–2516.
- [36] S.D. Ingale, P.D. Nemade, An investigation on fresh state properties of cement paste and concrete with GGBS and waste paper sludge ash, *Mater. Today: Proc.* 65 (2022) 1237–1242.
- [37] B. Nguyen Phan, R. Sekine, K. Hayano, H. Yamauchi, Assessment of consistency and strength properties of clays treated with paper sludge ash-based stabilizers using the water absorption and retention rate, *Constr. Build. Mater.* 351 (2022), 128936.
- [38] J. Zhang, P. Zheng, Q. Wang, Lime mud from papermaking process as a potential ameliorant for pollutants at ambient conditions: a review, *J. Clean. Prod.* 103 (2015) 828–836.
- [39] S. Zhou, Y. Ling, J. Zhao, Utilization of the Alkaline White Mud as Cement-Based Materials for the Production of Cement, *Journal of Civil & Environmental Engineering* 02 (01) (2012).
- [40] Y.i. Man, J. Li, M. Hong, Y. Han, Energy transition for the low-carbon pulp and paper industry in China, *Renew. Sustain. Energy Rev.* 131 (2020) 109998.
- [41] B.S. Gebregziabihier, R. Thomas, S. Peethamparan, Very early-age reaction kinetics and microstructural development in alkali-activated slag, *Cem. Concr. Compos.* 55 (2015) 91–102.
- [42] D. Jiang, X. Li, Y. Lv, C. Li, W. Jiang, Z. Liu, J. Xu, Y. Zhou, J. Dan, Autogenous shrinkage and hydration property of alkali activated slag pastes containing superabsorbent polymer, *Cem. Concr. Res.* 149 (2021), 106581.
- [43] H. Zhang, H. Yuan, Z. Ge, J. Wu, C. Fang, E. Schlangen, B. Savija, Fresh and hardened properties of self-compacting concrete containing recycled fine clay brick aggregates, *Mater. Struct.* 54 (4) (2021).
- [44] A.M. Rashad, W. Morsi, S.A. Khafaga, Effect of limestone powder on mechanical strength, durability and drying shrinkage of alkali-activated slag pastes, *Innov. Infrast. Solut.* 6 (2) (2021) 127.
- [45] C.K. Yip, G.C. Lukey, J.S.J. van Deventer, The coexistence of geopolymeric gel and calcium silicate hydrate at the early stage of alkaline activation, *Cem. Concr. Res.* 35 (9) (2005) 1688–1697.
- [46] I. Martínez-Lage, M. Velay-Lizancos, P. Vázquez-Burgo, M. Rivas-Fernandez, C. Vázquez-Herrero, A. Ramirez-Rodriguez, M. Martín-Cano, Concretes and mortars with waste paper industry: Biomass ash and dregs, *J. Environ. Manage.* 181 (2016) 863–873.
- [47] V. Ferrández-Mas, T. Bond, E. García-Alcocel, C.R. Cheeseman, Lightweight mortars containing expanded polystyrene and paper sludge ash, *Constr. Build. Mater.* 61 (2014) 285–292.
- [48] F. Puertas, A. Fernandez-Jimenez, Mineralogical and microstructural characterisation of alkali-activated fly ash/slag pastes, *Cem. Concr. Compos.* 25 (2003) (2003) 287–292.
- [49] F. Puertas, S. MartóÁñez-RamóÁrez, S. Alonso, T. VaÁzquez, Alkali-activated fly ash slag cements Strength behaviour and hydration products, *Cem. Concr. Res.* 30 (2000) 1625–1632.
- [50] S.-D. Wang, K.L. Scrivener, Hydration products of alkali activated slag cement, *Cem. Concr. Res.* 25 (3) (1995) 561–571.
- [51] B. Walkley, R. San Nicolas, M.-A. Sani, G.J. Rees, J.V. Hanna, J.S.J. van Deventer, J.L. Provis, Phase evolution of C-(N)-A-S-H/N-A-S-H gel blends investigated via alkali-activation of synthetic calcium aluminosilicate precursors, *Cem. Concr. Res.* 89 (2016) 120–135.
- [52] S.A. Bernal, R.M. de Gutierrez, J.L. Provis, V. Rose, Effect of silicate modulus and metakaolin incorporation on the carbonation of alkali silicate-activated slags, *Cem. Concr. Res.* 40 (6) (2010) 898–907.
- [53] D.E. Ortega-Zavala, J.L. Santana-Carrillo, O. Burciaga-Díaz, J.I. Escalante-García, An initial study on alkali activated limestone binders, *Cem. Concr. Res.* 120 (2019) 267–278.
- [54] G. Millán-Corralles, J.R. González-López, A. Palomo, A. Fernandez-Jiménez, Replacing fly ash with limestone dust in hybrid cements, *Constr. Build. Mater.* 243 (2020) 118169.
- [55] R. Cao, B. Li, N. You, Y. Zhang, Z. Zhang, Properties of alkali-activated ground granulated blast furnace slag blended with ferronickel slag, *Constr. Build. Mater.* 192 (2018) 123–132.
- [56] M.S. Kim, Y. Jun, C. Lee, J.E. Oh, Use of CaO as an activator for producing a price-competitive non-cement structural binder using ground granulated blast furnace slag, *Cem. Concr. Res.* 54 (2013) 208–214.
- [57] Z. Jia, C. Chen, H. Zhou, Y. Zhang, The characteristics and formation mechanism of the dark rim in alkali-activated slag, *Cem. Concr. Compos.* 112 (2020) 103682.
- [58] M.B. Haha, B. Lothenbach, G. Le Saout, F. Winnefeld, Influence of slag chemistry on the hydration of alkali-activated blast-furnace slag — Part I: Effect of MgO, *Cem. Concr. Res.* 41 (9) (2011) 955–963.

- [59] J. He, W. Zheng, W. Bai, T. Hu, J. He, X. Song, Effect of reactive MgO on hydration and properties of alkali-activated slag pastes with different activators, *Constr. Build. Mater.* 271 (2021) 121608.
- [60] E. Bernard, W.J. Zucha, B. Lothenbach, U. Mäder, Stability of hydrotalcite (Mg-Al layered double hydroxide) in presence of different anions, *Cem. Concr. Res.* 152 (2022) 106674.
- [61] I. Ismail, S.A. Bernal, J.L. Provis, R. San Nicolas, S. Hamdan, J.S.J. van Deventer, Modification of phase evolution in alkali-activated blast furnace slag by the incorporation of fly ash, *Cem. Concr. Compos.* 45 (2014) 125–135.
- [62] I. Garcia-Lodeiro, A. Palomo, A. Fernández-Jiménez, D.E. Macphee, Compatibility studies between N-A-S-H and C-A-S-H gels. Study in the ternary diagram Na<sub>2</sub>O–CaO–Al<sub>2</sub>O<sub>3</sub>–SiO<sub>2</sub>–H<sub>2</sub>O, *Cem. Concr. Res.* 41 (9) (2011) 923–931.
- [63] F. Puertas, M. Palacios, H. Manzano, J.S. Dolado, A. Rico, J. Rodríguez, A model for the C-A-S-H gel formed in alkali-activated slag cements, *J. Eur. Ceram. Soc.* 31 (12) (2011) 2043–2056.
- [64] S. Puligilla, P. Mondal, Co-existence of aluminosilicate and calcium silicate gel characterized through selective dissolution and FTIR spectral subtraction, *Cem. Concr. Res.* 70 (2015) 39–49.
- [65] Y. Zuo, M. Nedeljković, G. Ye, Pore solution composition of alkali-activated slag/fly ash pastes, *Cem. Concr. Res.* 115 (2019) 230–250.
- [66] C. Shi, R.L. Day, A Calorimetric Study of Early Hydration of Alkali-Slag Cements, *Cem. Concr. Res.* 25 (6) (1995) 1333–1346.
- [67] M.J. DeJong, F.-J. Ulm, The nanogranular behavior of C-S-H at elevated temperatures (up to 700 °C), *Cem. Concr. Res.* 37 (1) (2007) 1–12.
- [68] T. Lopez, P. Bosch, M. Asomoza, R. Gomez, E. Ramos, DTA-TG14 and FTIR spectroscopies of sol-gel hydrotalcites: aluminum source effect on physicochemical properties, *Mater. Lett.* 31 (1997) 311–316.
- [69] R. Sun, C. Fang, H. Zhang, Y. Ling, J. Feng, H. Qi, Z. Ge, Chemo-mechanical properties of alkali-activated slag/fly ash paste incorporating white mud, *Constr. Build. Mater.* 291 (2021) 123312.
- [70] P. Parashar, V. Sharma, D.D. Agarwal, N. Richhariya, Rapid synthesis of hydrotalcite with high antacid activity, *Mater. Lett.* 74 (2012) 93–95.
- [71] F. Demir, B. Dönmez, H. Okur, F. Sevim, Calcination Kinetic of Magnesite from Thermogravimetric Data, *Chem. Eng. Res. Des.* 81 (6) (2003) 618–622.
- [72] E. Adesanya, K. Ohenoja, T. Luukkonen, P. Kinnunen, M. Illikainen, One-part geopolymer cement from slag and pretreated paper sludge, *J. Clean. Prod.* 185 (2018) 168–175.
- [73] X. Gao, Q.L. Yu, H.J.H. Brouwers, Reaction kinetics, gel character and strength of ambient temperature cured alkali activated slag–fly ash blends, *Constr. Build. Mater.* 80 (2015) 105–115.
- [74] Z. Jia, C. Chen, H. Zhou, Y. Zhang, The characteristics and formation mechanism of the dark rim in alkali-activated slag, *Cem. Concr. Compos.* 112 (2020), 103682.
- [75] Y. Zhang, M. Liang, Y. Gan, O. Çopuroğlu, Effect of MgO content on the quantitative role of hydrotalcite-like phase in a cement-slag system during carbonation, *Cem. Concr. Compos.* 134 (2022), 104765.
- [76] A. Fernández-Jiménez, A. Palomo, Composition and microstructure of alkali activated fly ash binder: Effect of the activator, *Cem. Concr. Res.* 35 (10) (2005) 1984–1992.
- [77] R.J. Myers, S.A. Bernal, R. San Nicolas, J.L. Provis, Generalized structural description of calcium-sodium aluminosilicate hydrate gels: the cross-linked substituted tobermorite model, *Langmuir* 29 (17) (2013) 5294–5306.
- [78] J.S.J. van Deventer, R. San Nicolas, I. Ismail, S.A. Bernal, D.G. Brice, J.L. Provis, Microstructure and durability of alkali-activated materials as key parameters for standardization, *J. Sustain. Cem. Based Mater.* 4 (2) (2014) 116–128.